

Analysis of an Interplanetary Coronal Mass Ejection by a spacecraft radio signal: A case study.

G. Molera Calvés^{1,2,3}, E. Kallio², G. Cimò^{3,5}, J. Quick⁴, D.A. Duev^{6,3}, T.

Bocanegra Bahamón^{3,7,8}, M. Nickola⁴, M.A. Kharinov⁹, and A.G. Mikhailov⁹

Tracking radio communication signals from planetary spacecraft with ground-based telescopes offers the possibility to study the electron density and the interplanetary scintillation (IPS) of the solar wind. Observations of the telemetry link of planetary spacecraft have been conducted regularly with ground antennae from the European VLBI Network (EVN), aiming to study the propagation of radio signals in the solar wind at different solar elongations and distances from the Sun. We have analyzed the Mars Express spacecraft radio signal phase fluctuations while, based on a 3D heliosphere plasma simulation, an Interplanetary Coronal Mass Ejection (ICME) crossed the radio path during one of our observations on 2015.04.06. Our measurements showed that the phase scintillation indices increased by a factor of four during the passage of the ICME. The method presented here confirms that the phase scintillation technique based on spacecraft signals provides information of the properties and propagation of the ICMEs in the heliosphere.

1. Introduction

Interplanetary Coronal Mass Ejections (ICMEs) are a manifestation of active processes in the Sun where a substantial amount of matter is released from the outer atmosphere

G. Molera Calvés, guifre.moleracalves@nls.fi

¹Finnish Geospatial Research Institute,
National Land Survey of Finland, 02430
Masala, Finland.

²Aalto University, School of Electrical
Engineering, Dep. of Electronics and
Nanoengineering, 02150 Espoo, Finland.

³Joint Institute for VLBI ERIC, 7991 PD
Dwingeloo, The Netherlands.

⁴Hartebeesthoek Radio Astronomy
Observatory, 1740 Krugersdorp, South
Africa.

⁵ASTRON, The Netherlands Institute for
Radio Astronomy, 7990 AA Dwingeloo, The
Netherlands.

⁶California Institute of Technology, 91125
Pasadena, California, USA.

as Coronal Mass Ejections, CMEs [*Chen, 2011*] to the heliosphere. These large-scale magnetic structures [*Gosling, 1990; Cane and Richardson, 2003*] are one of the most important space weather phenomena as they can cause large geomagnetic storms on Earth.

An extreme Earth-directed ICME is also a potential hazard for man-made devices, such as satellites, communication lines or power grids. Characterizing the properties of ICMEs is therefore a very important field of research in heliospheric and magnetospheric physics, and in space physics in particular.

Measuring the properties of ICMEs in situ is, however, difficult because this would require multiple spacecraft around the heliosphere. For this reason, it is of interest to look for remote sensing methods for characterizing ICMEs, such as the coronagraphs in the missions of the SOLar and Heliospheric Observatory, SOHO [*Domingo et al., 1995*], and the Solar TERrestrial RELations Observatory, STEREO [*Kaisler et al., 2011*]. However,

⁷Department of Astrodynamics and Space

Missions, Delft University of Technology,
2629 HS Delft, The Netherlands.

⁸Shanghai Astronomical Observatory,
Chinese Academy of Sciences, 200030
Shanghai, China.

⁹Institute of Applied Astronomy of
Russian Academy of Sciences, 191187 St.
Petersburg, Russia.

remote observations have further limitations since ICMEs are often observed to be strongly deflected in both longitude and latitude as they depart from the corona [*Kay et al.*, 2015].

This complicates the estimation of whether an ICME would hit the Earth.

The amplitude and phase of any natural or man-made signal are disturbed when crossing an ICME. Natural radio sources have, for several decades, provided a tool to investigate heliospheric plasma by measuring interplanetary scintillation (IPS) (see e.g. *Hewish et al.* [1964]; *Jackson et al.* [1998]; *Kojima et al.* [1989]), by comparing radio observations with solar and heliospheric images (see e.g. *Jones et al.* [2007]; *Dorrian et al.* [2008]; *Hardwick et al.* [2013]), by in situ solar wind observations (see e.g. *Coles et al.* [1978]), and by simulating the plasma of the heliosphere (see e.g. *Sokól et al.* [2013]; *Kim et al.* [2014]).

Measurements of phase scintillation using radio signals of human origin transmitted by a spacecraft provides an additional tool to measure solar corona, heliosphere plasma, CMEs and ICMEs by radio tracking techniques at ground stations (see e.g. *Bird et al.* [1994, 1996]; *Pätzold et al.* [2012]; *Karl et al.* [1997]; *Molera Calvés* [2012]; *Duev et al.* [2016]).

Observations of planetary spacecraft have been carried out systematically since 2009 by the Planetary Radio Interferometry and Doppler Experiment (PRIDE) team by means of Very Long Baseline Interferometry (VLBI) instrumentation on ground radio telescopes [*Duev et al.*, 2012; *Molera Calvés*, 2012]. The propagation of the radio signal in the interplanetary medium have been used to estimate the electron density fluctuations in the solar wind [*Molera Calvés et al.*, 2014]. The campaign focused on tracking ESA's Venus Express (VEX) spacecraft from 2009 to 2014 (until mission termination),

ESA's Mars Express (MEX) spacecraft, from the beginning of 2014 onwards, and ESA's Rosetta comet spacecraft, from the beginning of 2015 to 2016 (until mission termination).

This study presents the analysis of variations in the radio communications signal transmitted by the MEX spacecraft in April 2015 as it propagated through the interplanetary plasma during the passage of a ICME across the line-of-sight. The method presented is sensitive to changes in the total electron column (TEC) density between the spacecraft and the Earth caused by the ICME. Electron density fluctuations can be used to characterize the properties of the ICME, such as size, structure, intensity and propagation speed.

The paper is organized as follows: first, the technique used to process the spacecraft signals is introduced in detail in Section 2.2. Second, the analysis of the data that led us to detect an ICME on the line-of-sight is described in Section 2.3. After that follows a description in Section 3 of how to characterize the properties of the ICME using data observed from two radio telescopes. Finally, the capability of a network of radio antennae to monitor similar events in the near future is discussed in Section 4.

2. Method and observations

2.1. Theory

The TEC between the spacecraft target and the Earth is defined as the integral of the electron density along the line-of-sight

$$\text{TEC} = \int_{\text{Earth}}^{\text{spacecraft}} n_e(R) \cdot dl, \quad (1)$$

where $n_e(R)$ is the electron density, which depends on the distance from the Sun (R).

Several studies can be found in the literature about the estimation of the electron density along the line-of-sight. In this research, we have used the electron density model for a *slow* solar wind as described in *You et al.* [2012]. In the paper we assign TEC_n as the TEC calculation based on You's density model.

The analysis of spacecraft radio signals allows one to determine the variation of the phase of a radio signal which is related to the variations in the electron density (δn_e) (see more in Sect. 2.2). In *Molera Calvés et al.* [2014], we presented a study based on observations of Venus Express with VLBI radio telescopes. In that paper we established, as stated in previous studies [*Coles et al.*, 1978; *Woo et al.*, 1996, 1995], that the *phase scintillation index* (σ_{Sc}) is approximately proportional to the interplanetary plasma TEC

$$TEC \propto \sigma_{Sc}, \quad (2)$$

where σ_{Sc} is a measure of the level of fluctuations in the phase of the spacecraft signal caused by the propagation in a turbulent media. The σ_{Sc} is defined as the standard deviation of the measured phase of the signal. The PRIDE group has conducted hundreds of observations since 2009 to establish a relationship between the TEC and the phase scintillation index at any given solar elongation. This relationship is summarized by the expression [*Molera Calvés*, 2012]

$$TEC_{\sigma_{Sc}} = 2 \cdot K_s \cdot \sigma_{Sc} \cdot \left(\frac{f_{obs}}{8.4\text{GHz}} \right) \cdot \left(\frac{300\text{s}}{\tau} \right)^{\frac{m+1}{2}}, \quad (3)$$

where $\text{TEC}_{\sigma_{Sc}}$ is expressed in total electron content units ($1\text{tecu} = 10^{16}$ electrons/m²).

The parameter K_s [tecu/rad] is an empirically determined constant based on observational data from spacecraft. These hundreds of observations have yielded to obtain one value for K_s with data from VEX and another one with data from MEX. They are based on several hundreds of observations conducted over 8 years. Thus, they cover all conditions of slow and fast winds, as well as, a wide range of solar elongations and Earth-spacecraft distances [Molera Calvés et al., 2014]. Continuing in Eq. 3, f_{obs} is the communications frequency of the spacecraft [GHz], which usually lies between 8.30 and 8.50 GHz, τ is the integration time [s] (typically τ is 300 s), m is the spectral index (based on the observations by Molera Calvés et al. [2014] m is approximately $-8/3$, which is consistent with a Kolmogorov power spectrum of fluctuations [Kolmogorov, 1991]), and σ_{Sc} is the phase scintillation index [rad] retrieved from the observations conducted by the radio telescopes. f_{obs} , τ and m allow us to adjust the equation depending on the spacecraft and the measurement results. However, in the standard VEX or MEX observations those terms cancel themselves out. A factor of 2 is included to take into account the two-way link between the Earth and the spacecraft. In this paper we refer to $\text{TEC}_{\sigma_{Sc}}$ as the TEC derived from the phase scintillation index as per Eq. 3.

2.2. Processing of the radio signal

The set-up of our observations is known as *three-way* radio link, where the radio signal transmitted by a spacecraft to a ground-station telescope is tracked by a secondary radio telescope [Asmar et al., 2005]. The spacecraft and the ground station operate in the so-called *two-way* mode, where the ground-telescope transmits a signal to the spacecraft and receives it back. Meanwhile the second telescope detects the signal and compares it

to a locally generated frequency. The VLBI radio telescopes use independent Hydrogen masers as their reference clock.

Sessions are planned accordingly to the transmission schedule provided by the mission support team. The antenna schedules are then prepared for the available telescopes. Data are recorded locally at the telescope and transferred off-line to the processing centre, minutes after the end of the session. The data processing is conducted at the Joint Institute for VLBI-ERIC (Dwingeloo, The Netherlands) and at the Aalto University Metsähovi Radio Observatory (Espoo, Finland).

The narrow-band data processing of the single dish open-loop data collected by the radio telescopes is divided into three blocks, as shown in Fig. 1: the SWSpec, SCTracker and digital PLL software (<https://github.com/gofrito/swspec>) [Molera Calvés, 2012].

SWSpec extracts the raw data from the channel where the spacecraft carrier tone is recorded, then it performs a window-overlapped add (WOLA) Discrete Fourier Transform (DTF) and an integration over the obtained spectra. The result is an initial estimate of the spacecraft carrier tone Doppler residual along the scan. The moving phase of the carrier tone throughout the scan is modelled by performing an n -order frequency polynomial fit. We have fitted the data with a polynomial of order 6 through the entire research.

SCTracker uses this initial fit to stop the phase of the carrier tone, allowing subsequent tracking, filtering and extraction of the carrier tone in a narrower band (from the initial 16 MHz channel bandwidth down to a 2 kHz bandwidth), using a second-order WOLA DFT-based algorithm of the Hilbert transform approximation. The digital Phase-Locked-Loop (dPLL) performs high-precision iterations of the previous steps – time-integration of the overlapped spectra, phase polynomial fitting and phase-stopping correction – on the

2 kHz bandwidth signal. The output of the dPLL is the filtered and down-converted signal, and the residual phase in the stopped band with respect to the initial phase polynomial fit. The bandwidth of the output detections is 20 Hz with a frequency spectral resolution of 2 mHz. The Doppler residual is obtained by adding the base frequency of the selected channel to the 10 s averaged carrier tone frequencies after the dPLL. For more details see [Molera Calvés et al., 2014].

The outputs of this analysis are the fluctuations of the recorded Doppler residual and the residual phase variations of the signal for the particular line-of-sight (Earth-spacecraft) in intervals of 20 minutes. The accuracy of the detections of the Doppler residual and the fluctuations in the signal phase allow us to extrapolate the electron density variations.

2.3. Radio observations

In April 2015, three consecutive sessions targeting MEX were conducted with the same radio telescope, the 15-metre antenna at the Hartebeesthoek radio astronomy observatory (Ht, South Africa). These observations were carried out under different weather conditions: the first day under heavy clouds, the second with strong wind and rain, and the last with clear sky. As described in Molera Calvés et al. [2014], the atmospheric conditions have little influence on the results. The results indicated that the worst measurement in terms of detection accuracy of the spacecraft signal was achieved with clear sky, on 2015.04.06.

This session consisted of tracking the MEX signal with the South African antenna and the Badary 32-metre radio telescope (Bd, Russia). Hence, we decided to investigate further what might have occurred during this session. Badary observed MEX from 05:00 to 08:40, while Ht observed from 07:20 to 08:40. So, there were overlapping observations

for 80 minutes (4 scans). The summary of the observations conducted around the vicinity of 2015.04.06 is shown in Table 1.

Badary's observation yielded similar results to those at Hartebeesthoek, being namely the phase scintillation higher than in standard conditions. The matching of results between both radio telescopes suggested that a plasma anomaly, later identified as an ICME, may have been detected.

Figure 2 compares the detection in frequency terms of the MEX radio signal before, during and after the ICME. The upper plot shows the Doppler residual of the full session observed on 2015.04.04 (blue line) and 2015.04.06 (red line) at the Hartebeesthoek station. The lower panel shows the residuals measured on 2015.04.06 (red line) and 2015.04.09 (blue line) at the Badary telescope. It is clear from Fig. 2 that the fluctuations of the Doppler residuals are much higher for the analyzed ICME than similar measurements collected in its vicinity.

The drastic change on the behaviour of the radio signal during the ICME can be better seen in the plot of the residual phase of the signal. Figure 3 shows the residual phase measured at Hartebeesthoek (upper panel) on 2015.04.04 (blue line) and 2015.04.06 (red line), and at Badary (lower panel) on 2015.04.06 (red line) and on 2015.04.09 (blue line). Several scans during the ICME pass show phase fluctuations that are ten times higher than during undisturbed solar wind conditions. The data provided on 2015.04.09 reflects nominal conditions, since the results are in good agreement with spacecraft data collected since 2009. For comparison, the initial time is assumed to be the same and the x -axis shows the relative time with respect to the beginning of the sessions. The periodicity seen in the residual phase is a known feature due to of the extraction method.

The spectral signature of the phase fluctuations is another valid way to look at the results. The level of the scintillation can be extrapolated by estimating the integral of the spectral power density of the phase fluctuations [Molera Calvés et al., 2014]. The spectral power density of the phase fluctuations for sessions with Hartebeesthoek on 2015.04.04 (green line) and 2015.04.06 (blue line), and with Badary on 2015.04.06 (violet line) and 2015.04.09 (red line) are shown in Fig. 4. The peaks of the power spectra in both sessions observed on 2015.04.06 are two orders of magnitude higher than in the other two.

The Doppler residuals, phase fluctuations and spectral signature statistics for these observations are summarised in Table 2. For the estimates, we used the f_{obs} of MEX which is equal to 8.421 GHz, an integration time of 5 min, and the value of K_s empirically found by spacecraft observations collected from MEX data (from 2014 to 2016) [Molera Calvés et al., 2014]. The K_s factor from over 450 observations on MEX is approximately 2010 *tecu*/rad.

3. Interpretation of the observations

3.1. CME simulations and in situ observations

CACTUS online software (<http://sidc.oma.be/cactus/>) registered a solar eruption produced on the surface of the Sun at 23:48 UTC on 2015.04.04. This solar eruption evolved into a flare of an intensity of type C and with a coronal mass ejection. This CME (internal reference number: 0012) propagated with an angle of emission with respect to North of 115° and an angular width of 176° . The average speed of the ICME was 400 km/s, with a minimum and maximum velocity of 103 and 1358 km/s. Further information about the ICME is available online at the Integrated Space Weather Analysis System (iSWA, <http://iswa.gsfc.nasa.gov/>).

The ICME propagated towards a latitude of -3° in the elliptic plane. According to the computer simulation, shown in Fig. 5, almost 24 hours later, at 00:00 UTC on 2015.04.06, the ICME crossed the line-of-sight (shown by a black arrow) between Mars (red circle) and Earth (yellow circle). The Badary radio telescope started the observations at 05:00 UTC. The radio communications signal between Mars Express and the ground station of New Nortia crossed the ICME in both directions. At that time, Mars was at a solar elongation of 17.23° and a distance of 2.39 AU with respect to the Earth. Meanwhile, the ICME was at a distance of 0.5-0.6 AU from the Sun or at $1/5$ of the path between the spacecraft and the observer, moving towards the latter.

Based on the computer simulation in Fig. 5, we estimate that the radio signal intersected the plasma cloud with an approximate angle of incidence of 12° . The simulation covers the time of our observations (2015.04.06 at 06:00 UTC) when the ICME is present between Mars and Earth. The ENLIL simulations were prepared by the Community Coordinated Modelling Center (CCMC) at Goddard space center and are available through the Integrated Space Weather Analysis System (iSWA, <https://ccmc.gsfc.nasa.gov/iswa/>). The electron density and the radial speed of the solar wind in the ecliptic plane (as based on a computer simulation at the time of the observations) are presented in the left and right panel, respectively.

3.2. Interpretation of the radio observations

On 2015.04.04-03, the observations were carried out in the evening, when the spacecraft was locked to the ESA ground station in Malargüe (Argentina). The other data sets were collected in the morning, when the spacecraft was locked to the ESA ground station in New Nortia (Australia). The European Space Operations Centre (ESOC) confirmed that no

data anomalies were encountered on the transmitting pipeline during the aforementioned days. Therefore, it was confirmed that the signal disturbance analyzed in this paper was not introduced during the transmission phase.

It was important to analyze how the different azimuth and elevations values affected the ionospheric and solar wind TEC contributions and, therefore, might have influenced our Doppler measurements. To estimate the contribution of the Earth's ionosphere, we used the vertical TEC (vTEC) maps provided by the International GSS Service (IGS) on the basis of post-processing global GNSS (GPS and GLONASS) observations. The IGS fits the GNSS data to the single thin ionospheric layer model to estimate the vTEC values on a global grid with a spacial resolution of 5° in longitude and 2.5° in latitude and a two-hour temporal resolution. Detailed description of the ionospheric post-processing can be found in *Duev et al.* [2012].

Next, we estimated the expected TEC contribution of the solar wind under undisrupted conditions. We used the approach described by *You et al.* [2012] that takes into account the electron density models for fast and slow solar winds. The two-way interplanetary plasma TEC is corrected for the up- and downlink frequency ratio at X-band by a factor of $1 + 880/749$ [*Armstrong, 1998*]. Table 3 shows the TEC contribution for the ionosphere uplink (ground station - spacecraft), and downlink (spacecraft - VLBI radio telescope), and the solar wind (TEC_n).

As can be seen from Table 3, the ionospheric values were relatively steady during the observations: values varying between 40 and 100tecu . Ionospheric TEC fluctuations are much smaller than changes seen in the solar wind TEC model. This also suggested that the

fluctuations in our data were generated in space by some high density plasma phenomena, such as an ICME, which moved through the line-of-sight and not by the ionosphere.

Once the detection of an ICME in the radio signal observed by our radio telescopes was verified as seen in Sect. 3.1, we characterised and studied its properties. First, we analyzed the phase scintillation indices and Doppler measurements independently for each of the four scans observed at Hartebeesthoek and the ten scans observed at Badary. Table 4 presents the main statistics for all scans observed on 2015.04.06. The average σ_{Sc} from Hartebeesthoek and Badary data were 1.537 rad and 2.170 rad, respectively.

Table 4 shows the high variability of the results within the session. Both the Doppler accuracy and the phase scintillation index show a high standard deviation amongst the samples. In normal observations dispersion is common, however, not at the levels presented here. The spectral slope, the spectral peak and the noise level are estimated using the Spectral power plot (see Fig. 4) and represent the average of all scans observed within one session.

The Doppler residuals, the σ_{Sc} measurement for the three hours of the session at both radio telescopes are shown in Fig. 6. The upper panel presents the measurements of Doppler accuracy for each 20-minute scan. The data from Badary is plotted with blue stars and from Hartebeesthoek in red circles. Measurements from Hartebeesthoek telescope are displaced because the antenna started observing two hours later than Badary. The lower panel presents the measurements of the phase scintillation index using the same colour scheme. As seen in the graphs, a similar feature is present on the data sets from both radio telescopes at the same time, eliminating a possible instrumental effect from the stations. The measurement errors have been included in both cases.

We estimated the expected TEC along the line-of-sight based on our measurements (defined as $TEC_{\sigma_{Sc}}$ from Eq. 3), using the data presented in Table 4. As the observations and the processing was conducted in our standard mode (i.e. $f_{obs}=8.421$ GHz and $\tau=300$ s) Eq. 3, gets the form

$$TEC_{\sigma_{Sc}} = 2 \cdot K_s \cdot \sigma_{Sc}, \quad (4)$$

where K_s is $2010\text{tecu}/\text{rad}$ in the case of MEX data (as discussed in Sect. 2.3) and the values of σ_{Sc} are given in Table 2. The average value of the σ_{Sc} measurements from all scans observed at Hartebeesthoek and Badary telescopes were 1.537 rad and 2.170 rad, respectively. Thus, the estimated $TEC_{\sigma_{Sc}}$ is equal to 3430tecu for Hartebeesthoek and 4340tecu for Badary. The expected TEC_n value based on [You et al., 2012] model, as was shown in Table 3, was 1357tecu . We assumed that the measured TEC, which is 2.5 times higher in the case of Hartebeesthoek and 3.5 times in the case of Badary than the expected TEC values, is caused by to the presence of the ICME along the line-of-sight.

3.3. ICME density profile

To evaluate the effect of the ICME on the spacecraft signal we generated a 2D model of the electron density/content along the line-of-sight. The model is based on two inputs: the simulation of the electron density estimated from the ENLIL simulation (Fig. 5) and the electron density model from You et al. [2012] (Fig. 7).

The dashed line in Fig. 7 shows the electron density model of the undisturbed solar wind (TEC_n). The solid line shows the solar wind while adding the simulation of the ICME. In order to model the effect of the ICME, we have taken a 1D section along the

line-of-sight of the of the electron density map of Fig. 5 (left panel) and reconstructed its smoothed density profile. The total electron content model including the ICME model is referred to in this paper as TEC_{nc} .

Table 5 compares the two simulations of the electron content model along the line-of-sight based on the measurements from the two radio telescopes. TEC_n is the undisturbed solar wind based on *You et al.* [2012] model, TEC_{nc} the integral of the 2D electron density profile with the ICME shown in Figure 7, and $TEC_{\sigma_{sc}}$ is based on the data collected at each radio telescope.

The different TEC values between the models and the measurements obtained by the radio telescopes are probably related to the propagation and inner structure of the ICME. Studies have been carried out to examine their properties and explain their propagation in the heliosphere [*Liu et al.*, 2008; *Davis et al.*, 2009]. These studies suggest that the ICME contains two components: a shockwave moving at high speed, dense plasma density and tenous magnetic field, and a cavity moving at lower speed, weak plasma density, but stronger magnetic field. Our studies showed that the modeled TEC_{nc} is lower than the measured $TEC_{\sigma_{sc}}$, which could be caused by different values of K_s in these two cases. Therefore, there is no guarantee that the average value of K_s , calculated for the general case (Eq. 3), is appropriate for ICMEs. How the K_s may differ in these two regions is not yet known. Furthermore, in *Molera Calvés* [2012] it was argued that 20-minutes of observational data was enough to characterise to outer scale of turbulences assuming typical speed of plasma inhomogeneties. However, due the nature of the inner part of the ICME the scaling parameter K_s would be sensitive to velocity changes. Recently, *Pätzold et al.* [2012] studied the general structure of CMEs by using radio occultation measurements

and compared it to the electron column density variations. In their model a large-scale density variation occurs only once in the sheath region of the CME, meanwhile a small density peak associated with the shock precedes the sheath region.

One natural question to ask is whether we can derive information about the inner structure of the ICME based on these observations. According to the ENLIL simulation (Fig. 5) the velocity of the ICME is approximately of the order of 700 km/s. The total time-span during which the radio signal crosses the large disturbance region inside of the ICME is about 50 min (see Fig. 6). The distance travelled by the ICME during this period is therefore about 0.014 AU, or about 10% of the size of the ICME as estimated from Fig. 5. Figure 8 shows an illustration of a feasible simple model for the structure of this ICME.

We associate the first peak seen in the phase scintillation measurements at around 05:00 to the transit of the transmitted radio signal through the sheath of the ICME (a). The peak is immediately followed by a bump which we attribute to the signal propagating through the plasma cloud/density enhancement with very high density region (b). The electron column fluctuations reduce when the radio signal propagates only through the sheath of the ICME again (c).

We can speculate that the spacecraft signal has passed transversally through a plasma cloud with very high density inside the ICME between the shockwave and the tail, which drastically enhances the disturbance of the signal. Why this high density region would have resulted such a strong disturbance and how to quantify it is unclear. Unfortunately, we do not have enough information to associate this high density layer directly with the ICME's cloud. It is finally worth noting that the results of the frequency and phase

variation analysis are similar to those presented recently by *Pätzold et al.* [2012] and *Ando et al.* [2015].

3.4. Cross correlation of the residual phase

In addition to the analysis presented above, it should be possible, at least on a theoretical point of view, to derive more information on the ICME by cross-correlating the residual phases. Following the work done by *Efimov et al.* [2008, 2009], we attempted to cross-correlate the phase of the signal recorded at the two telescopes. Such a correlation would retrieve parameters of the time lag and plasma speed of the ICME. In our case, the telescopes observed simultaneously for the last four scans, i.e. 80 min. The sampling time was 25 milliseconds. The initial times for each of the four scans were different but were subsequently correctly realigned.

However, we did not succeed in correlating the residual phases. The distance between the telescopes was probably too large: 9000 km North-South and 5000 km East-West. This would require, for proper correlation, a strong extra-galactic source as phase calibrator [*Beasley and Conway, 1995*]. The use of such a source as phase-reference will be considered in future observations.

4. Conclusions

This paper describes the detection of an Interplanetary Coronal Mass Ejections (ICME) using the two-way radio communications link between a planetary spacecraft and ground radio telescopes. Our technique measured a phase scintillation index three times higher when crossing the ICME than during undisturbed solar wind conditions. Radio tracking is a valuable technique to study the properties of ICMEs with ground-based observations.

In our study we calculated the TEC of the plasma anomaly, which is more than 3000 $tecu$ (see Table 5). Furthermore, we estimated using a simplified description the size of the internal structure of the ICME observed, which was to be around 0.014 AU. It is worth noticing that the probability of detection of an ICME is low: over the past seven years and 500 observations only one such event has been detected.

In the future, using several spacecraft around the heliosphere, for example small size CubeSatellites, it would be possible to make a 2D or a 3D tomography of the heliosphere by using the multiples lines of sight between the Earth and the satellites. However, even now, real-time observations of ICME events are possible, provided that there is a quick reaction to strong flare spots on the Sun, a suitable spacecraft-Earth-CME geometry and rapid coordination with a radio telescope. Use of radio telescopes that already monitor 24/7 for possible solar flares, could allow real-time observations studying ICMEs and their propagation.

Future analysis of ICMEs could be improved in three ways. i) by the use of more detailed modelling of the density within the ICME taking into account its 3D motion and orientation. Moreover, about 30% of the registered ICMEs contain also magnetic cloud-like structures [*Cane and Richardson, 2003*], and those 3D structures could also be modelled. ii) by the addition in situ ICME plasma or magnetic field measurements by a planetary spacecraft (see e.g. *Futaana et al. [2008]*; *Kubicka et al. [2016]*) to remote sensing radio wave observations. iii) by conducting longer observations that cover the entirety of the pass of the ICME, it would be possible to measure precisely its effect before, during, and after the event.

Overall, this study suggests that spacecraft radio-link scintillation analysis can be used to detect ICMEs and to analyze their properties, especially, when the observations are integrated into global heliospheric models.

Acknowledgments. This work was made possible by observations conducted by a number of EVN radio telescopes. The EVN is a joint facility of European, Chinese, Russian, and South African institutes funded by their National Research Councils. The authors would like to thank all the station operators who conducted the observations, ESOC for their collaboration in planning the observations and ESA's MEX project team for their support and assistance. The authors would also like to acknowledge the ISWA for the ENLIL simulations and the data from the ACE spacecraft. T. Bocanegra Bahamón acknowledges the NWO–ShAO agreement on collaboration in VLBI.

The spacecraft tracking software is available at an online repository (bitbucket.org/spacevlbi/). The data presented in this paper are available at an online repository (bitbucket.org/spacevlbi/cme-monitoring).

References

- Ando, H., Shiota, D., Imamura, T., Tokumaru, M., Asai, A., Isobe, H., Patzold, M., Häusler B., and Nakamura, M. (2015). Internal structure of a coronal mass ejection revealed by Akatsuki radio occultation observations, *J. Geophys. Res.*, 120, 7, 5318-5328.
- Armstrong J.W. (1998). Radio wave Phase Scintillation and Precision Doppler Tracking of Spacecraft, *Radio Sci.*, Vol. 33, issue 6, p. 1727-1738.

Asmar, S.W., Armstrong, J.W., Iess, L., and Tortora, P. (2005). Spacecraft Doppler tracking: Noise budget and accuracy achievable in precision radio science observations, *Radio Sci.*, 40.

Beasley, A.J., and Conway, J.E. (1995). VLBI Phase-Referencing, eds. *ASP*, 82, 327.

Bird, M.K., Volland, H., Pätzold, M., Edenhofer, P., Asmar, S.W., and Brenkle, J.P. (1994). The Coronal Electron Density Distribution Determined from Dual-Frequency-Frequency Ranging Measurements during the 1991 Solar Conjunction of the Ulysses Spacecraft, *Astrophys. J.*, 426, 373-381.

Bird, M. K., Pätzold, M., Edenhofer, P., Asmar, S.W., and McElrath, T. P., (1996). Coronal radio sounding with Ulysses: solar wind electron density near 0.1AU during the 1995 conjunction, *Astron. & Astroph.*, vol. 316, p. 441-448.

Cane, H.V. and Richardson, I.G. (2003). Interplanetary coronal mass ejections in the near-Earth solar wind during 1996-2002, *J. Geophys. Res.*, 108(A4).

Chen, P.F. (2011). Coronal mass ejections: Models and their observational basis, *Living Rev. Solar Phys.*, 8(1).

Coles, W.A., Harmon, J.K., Lazarus, A.J., and Sullivan, J.D. (1978). Comparison of 74-MHz interplanetary scintillation and IMP 7 observations of the solar wind during 1973, *J. Geophys. Res.* 83(A7), 3337.

Davis, C.J., Davies, A., Lockwood, M., Rouillard, A.P., Eyles, C.J., and Harrison, R.A. (2009). Stereoscopic imaging of an Earth-impacting solar coronal mass ejection: A major milestone for the STEREO mission, *Geophys. Res., Lett.* 36, (8), L08102. doi:10.1029/2009GL038021.

Domingo, V., Fleck, B., and Poland, A.I. (1995). The SOHO mission: An overview, *Solar Phys.*, 162:1–37.

Dorrian, G.D., Breen, A. R., Brown, D.S., Davies, J.A., Fallows, R.A., and Rouillard A.P. (2008). Simultaneous interplanetary scintillation and Heliospheric Imager observations of a coronal mass ejection, *Geophys. Res. Lett.*, 35, L24104, doi:10.1029/2008GL036181.

Duev, D.A., Molera Calvés, G., Cimo, G., Bocanegra-Bahamon, T, Pogrebenko, S. V., and Gurvits L. I., (2012). Spacecraft VLBI and Doppler tracking: algorithms and implementation, *Astron. & Astroph.*, 541, A43.

Duev, D.A. Pogrebenko, S.V. , Cimo, G., Molera Calves, G., Bocanegra Bahamon, T., Gurvits, L.I., Kettenis, M.M, Kania, J., Tudose, V., Rosenblatt, P., Marty, J.-C., Lainey, V., de Vicente, P., Quick, J., Nickola, M., Neidhardt, A., Kronschnabl, G., Ploetz, C., Haas, R., Lindqvist, M, Orlati, A., Ipatov, A.V., Kharinov, M.A., Mikhailov, A.G., Lovell, J.E.J., McCallum¹⁹, J.N., Stevens, J., Gulyaev, S.A., Natush, T., Weston, S., Wang, W.H., Xia, B., Yang, W.J., Hao, L.-F., Kallunki, J., and Witasse, O. (2016). Planetary Radio Interferometry and Doppler Experiment (PRIDE) technique: A test case of the Mars Express Phobos fly-by, *Astron. & Astroph.*, 593, A34.

Efimov, A.I., Samoznaev, L.N., Bird, M.K., Chashei, I.V., and Plettemeier, D. (2008). Solar wind turbulence during the solar cycle deduced from Galileo coronal radio-sound experiments, *Adv. in Space Research*, vol. 42, p. 117-123.

Efimov, A.I., Armand, N.A., Lukanina, L.A., Samoznaev, L.N., Chashei, I.V., and Bird, M.K. (2009). Investigation of coronal mass ejections by the two-position radio sounding method, *Geomag. Aeron.*, 49 (8), 1165-1169.

Futaana, Y., et al., (2008). Mars Express and Venus Express multi-point observations of geoeffective solar flare events in December 2006, *Planet. Space Sci.* 56, 873-880.

Gosling, J.T. (1990). Geophysical monograph. In E. R. Priest, L. C. Lee, and C. T. Russel, editors, Coronal mass ejections and magnetic flux ropes in interplanetary space, 58, 343-364.

Jackson, B.V., Hick, P. L., Kojima, M., and Yokobe, A., (1998) Heliospheric tomography using interplanetary scintillation observations: 1. Combined Nagoya and Cambridge data, *J. Geophys. Res.*, vol. 103, A6, 12049-12067, DOI:10.1029/97JA02528

Jones, R. A., Breen, A. R., Fallows, R. A., Canals, A., Bisi, M. M., and Lawrence, G. (2007). Interaction between coronal mass ejections and the solar wind, *J. Geophys. Res.*, 112, A08107, doi:10.1029/2006JA011875.

Hardwick, S.A., Bisi, M.M., Davies, J.A., Breen, A.R., Fallows, R.A., Harrison, R.A., and Davis, C.J., (2013), Observations of Rapid Velocity Variations in the Slow Solar Wind, *Solar Phys.*, vol. 285, 111-126, doi:10.1007/s11207-013-0223-x

Hewish, A., Scott, P. F., and Wills, D. (1964) Interplanetary Scintillation of Small Diameter Radio Sources, *Nature*, 203, 1214-1217, doi:10.1038/2031214a0

Kaiser, M. L., Kucera, T. A., Davila, J. M., St. Cyr, O. C., Guhathakurta, M., and Christian, E. (2008). The STEREO mission: An introduction, *Space Sci. Rev.*, 136:5-16.

Karl, J., Pätzold, M. and Bird, M.K. (1997). Coronal Radio Sounding: NonGaussian Turbulence in the Source Regions of the Solar Wind, *Geophys. Res. Lett.* 24, 2881-2884.

Kay, C., dos Santos, L. F. G., and Opher, M. (2015). Constraining the Mass and the Non-Radial Drag Coefficient of a Solar Coronal Mass Ejection, *Astrophys. J.*, vol. 801,

Kim, T. K., Pogorelov, N. V., Borovikov, S. N., Jackson, B. V., Yu, H.-S., and Tokumaru, M. (2014). MHD heliosphere with boundary conditions from a tomographic reconstruction using interplanetary scintillation data, *J. Geophys. Res. Space Phys.*, 119, 7981-7997, doi:10.1002/2013JA019755.

Kojima, K., Tokumaru, M., Watanabe, H., Yokobe, A., Asai, K., Jackson, B.V., and Hick, P. L. (1998). Heliospheric tomography using interplanetary scintillation observations: 2. Latitude and heliocentric distance dependence of solar wind structure at 0.1-1 AU, *J. Geophys. Res.*, vol. 103, A2, 1981-1989, doi: 10.1029/97JA02162

Kolmogorov, A.N., (1991). Turbulence and stochastic processes: Kolmogorov's ideas 50 years on - The local structure of turbulence in incompressible viscous fluid for very large Reynolds numbers, *Proc. Royal Soc. London, Ser. A.*, 434, 9. doi:10.1098/rspa.1991.0075

Kubicka, M., Möstl, C., Amerstorfer, T., Boakes, P.D., Feng, L., Eastwood, J.P., and Törmänen, O. (2016). Prediction of geomagnetic storm strength from inner heliospheric in situ observations, *Astrophys. J.*, 833, 255. doi:10.3847/1538-4357/833/2/255

Liu, Y., Luhmann, J. G., Muller-Mellin, R., Choeder, P.C., Wang, L., Lin, R.P., Bale, S.D., Li, Y., Acuña, H., and Sauvaud, J.A. (2008). A comprehensive view of the 2006 December 13 CME: from the Sun to interplanetary space, *Astrophys. J.*, vol. 689, 563

Molera Calvés, G. (2012). Radio Spectroscopy and Space Science with VLBI Radio Telescopes for Solar System Research, PhD dissertation, Aalto University, Pub. No. 42/2012.

Molera Calvés G., Pogrebenko, S. V., Cimò, G., Duev, D. A., Bocanegra-Bahamón, T. M., Wagner, J. F., Kallunki, J., de Vicente, P., Kronschnabl, G., Haas, R., Quick, J., Maccaferri, G., Colucci, G., Wang, W. H., Yang, W. J., and Hao, L. F. (2014). Observations

and analysis of phase scintillation of spacecraft signal on the interplanetary plasma,
Astron. & Astroph., Vol. 564, A4, 7.

Pätzold, M., Hahn, M., Tellmann, S., Häusler B., Bird, M.K., Tyler, L., Asmar, S.W.,
and Tsurutani, B.T. (2012). Coronal density structures and CMEs: Superior solar con-
junctions of Mars express, Venus express, and Rosetta: 2004, 2006 and 2008, *Sol. Phys.*,
279, 127-152.

Sokól J.M., Bzowski, M., Tokumaru, M., Fujiki, K., McComas, D.J. (2013). Heliolatitude
and Time Variations of Solar Wind Structure from in situ Measurements and Interplane-
tary Scintillation Observations, *Solar Phys*, 285:167-200, doi:10.1007/s11207-012-9993-9

Woo, R., Armstrong. J.W., and Gazis, P.R. (1995). Doppler scintillation measurement of
the heliospheric current sheet and coronal streamers close to the Sun, Proceedings of
the 28th. ESLAB symposium.

Woo, R., Yang, F.-C., Yip, K. W., Kendall, W. B. (1976). Measurements of large-scale
density fluctuations in the solar wind using dual-frequency phase scintillations, *Astro-
phys. J.*, vol. 210, 568-574.

You, X.P., Coles, W.A., Hobbs, G.B. and Manchester, R.N. (2012). Measurement of the
electron density and magnetic field of the solar wind using millisecond pulsars, *MNRAS*,
Vol. 422, 1160-1165.

Table 1. Summary of the observations conducted of MEX in April 2015. Columns from left to right give the epoch (day.month.year), observing station (Ht - Hartebeesthoek, Bd - Badary), number of scans, weather conditions at the site, ESA's ground station (NNO - New Nortia, Australia, CEB - Cebreros, Spain), initial and ending time of the observations (in UTC), ranges of the azimuths and elevations tracked by the telescopes.

Epoch	Station	No. scans	Weather cond.	Ground station	Start Obs.	Stop Obs.	Azimuth	Elevation
2015.04.03	Ht	3	Cloudy	NNO	14:20	15:20	304°-297°	30°-22°
2015.04.04	Ht	3	Rainy	NNO	14:20	15:20	304°-297°	30°-22°
2015.04.06	Ht	4	Clear	CEB	07:20	08:40	65°-52°	22°-33°
2015.04.06	Bd	10	Clear	CEB	05:20	08:40	160°-225°	50°-43°
2015.04.09	Bd	14	Rainy	CEB	03:00	07:40	160°-250°	50°-33°

Table 2. Measurements obtained from five observations around 2015.04.06. The columns from the left to right are: epoch, name of the station (Ht: Hartebeesthoek; Bd: Badary), Doppler residual average, phase fluctuations average, spectral peak, phase scintillation index (σ_{Sc}) and $TEC_{\sigma_{Sc}}$.

Epoch	Station	Doppler mean	Phase fluctuations	Spectral peak	σ_{Sc}	$TEC_{\sigma_{Sc}}$
2015.04.03	Ht	5.1 ± 0.8 mHz	0.51 ± 0.11 rad	230 rad ² /Hz	0.482 rad	964 <i>tecu</i>
2015.04.04	Ht	6.9 ± 0.4 mHz	0.65 ± 0.07 rad	1153 rad ² /Hz	0.558 rad	1116 <i>tecu</i>
2015.04.06	Ht	19.1 ± 3.8 mHz	1.96 ± 0.59 rad	17477 rad ² /Hz	1.537 rad	3074 <i>tecu</i>
2015.04.06	Bd	19.7 ± 4.0 mHz	2.25 ± 0.56 rad	12550 rad ² /Hz	2.170 rad	4340 <i>tecu</i>
2015.04.09	Bd	4.3 ± 0.6 mHz	0.44 ± 0.10 rad	763 rad ² /Hz	0.512 rad	1024 <i>tecu</i>

Table 3. TEC estimations along the line-of-sight for the MEX observations in April 2015: Epoch, radio telescopes (Ht: Hartebeesthoek; Bd: Badary), ionospheric TEC for the ionospheric downlink (ground station - spacecraft) and the uplink (spacecraft-radio telescope), and the interplanetary plasma derived from You et al. for a slow wind model (TEC_n).

Observation		Total Electron Content [in <i>tecu</i>]		
Epoch	Station	Ionos Dw	Ionos Up	solar wind
2015.04.03	Ht	95.9	103.1	1299
2015.04.04	Ht	96.2	100.1	1320
2015.04.06	Ht	71.9	59.8	1357
2015.04.06	Bd	42.6	59.8	1356
2015.04.09	Bd	48.3	57.0	1423

Table 4. Parameters for each scan on 2015.04.06 with Hartebeesthoek (Ht) and Badary (Bd) radio telescopes: Initial time of the scan, the phase scintillation index (σ_{Sc} in rad), the slope of the spectral power density, the spectral peak (in rad^2/Hz) at 3 mHz, the noise level (in rad^2/Hz), the Doppler accuracy (in Hz) and relative signal-to-noise ratio (SNR).

Time	Station	σ_{Sc}	spectral slope	spectral peak	noise level	Doppler accuracy	SNR
05:20	Bd	2.568 ± 0.015	-2.828 ± 0.079	12550	1.28×10^{-4}	23.36	82471
05:40	Bd	2.014 ± 0.014	-2.828 ± 0.079	12550	1.28×10^{-4}	17.16	84111
06:00	Bd	2.179 ± 0.013	-2.828 ± 0.079	12550	1.28×10^{-4}	15.16	87518
06:20	Bd	1.328 ± 0.013	-2.828 ± 0.079	12550	1.28×10^{-4}	14.93	88385
06:40	Bd	3.013 ± 0.013	-2.828 ± 0.079	12550	1.28×10^{-4}	20.65	88059
07:00	Bd	2.836 ± 0.023	-2.828 ± 0.079	12550	1.28×10^{-4}	25.16	90772
07:20	Bd	3.053 ± 0.022	-2.828 ± 0.079	12550	1.28×10^{-4}	26.05	87260
07:40	Bd	1.847 ± 0.014	-2.828 ± 0.079	12550	1.28×10^{-4}	16.02	85675
08:00	Bd	1.995 ± 0.014	-2.828 ± 0.079	12550	1.28×10^{-4}	19.42	84859
08:20	Bd	1.654 ± 0.014	-2.828 ± 0.079	12550	1.28×10^{-4}	15.51	79284
07:20	Ht	2.983 ± 0.028	-2.744 ± 0.114	17477	3.24×10^{-4}	25.43	24603
07:40	Ht	1.750 ± 0.021	-2.744 ± 0.114	17477	3.24×10^{-4}	16.22	25394
08:00	Ht	1.537 ± 0.021	-2.744 ± 0.114	17477	3.24×10^{-4}	16.97	25914
08:20	Ht	1.604 ± 0.021	-2.744 ± 0.114	17477	3.24×10^{-4}	16.41	26632

Table 5. Estimated TEC values using three solar wind density methods: (i) undisturbed solar wind contribution based on *You et al.* [2012] model (TEC_n), (ii) integral of the 2D electron profile derived from the ICME simulation in Fig. 7 (TEC_{nc}), (iii) and our estimation based in the phase scintillation index and Eq. 3 from Harteesthoek (Ht) and Badary (Bd) telescopes. ($TEC_{\sigma_{Sc}}$).

Symbol	Definition	TEC
TEC_n	<i>You et al.</i> [2012] n_e model without the ICME	1350 <i>tecu</i>
TEC_{nc}	electron profile with the ICME	1950 <i>tecu</i>
$TEC_{\sigma_{Sc}}(Ht)$	derived from σ_{Sc} Ht measurements	3430 <i>tecu</i>
$TEC_{\sigma_{Sc}}(Bd)$	derived from σ_{Sc} Bd measurements.	4350 <i>tecu</i>

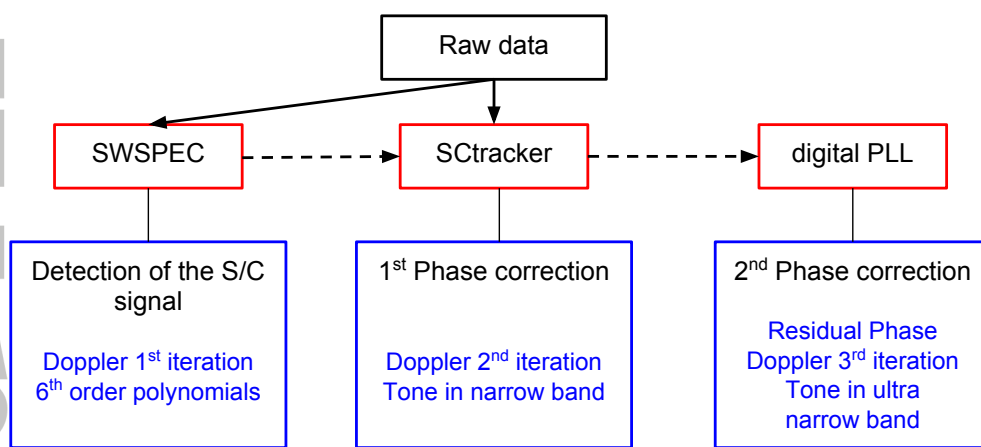


Figure 1. Illustration of the data analysis steps and software modules used for spacecraft tracking purposes: SWspec, SCtracker and digital Phase-Locked-Loop. All the software is developed and maintained jointly by JIVE and Aalto University.

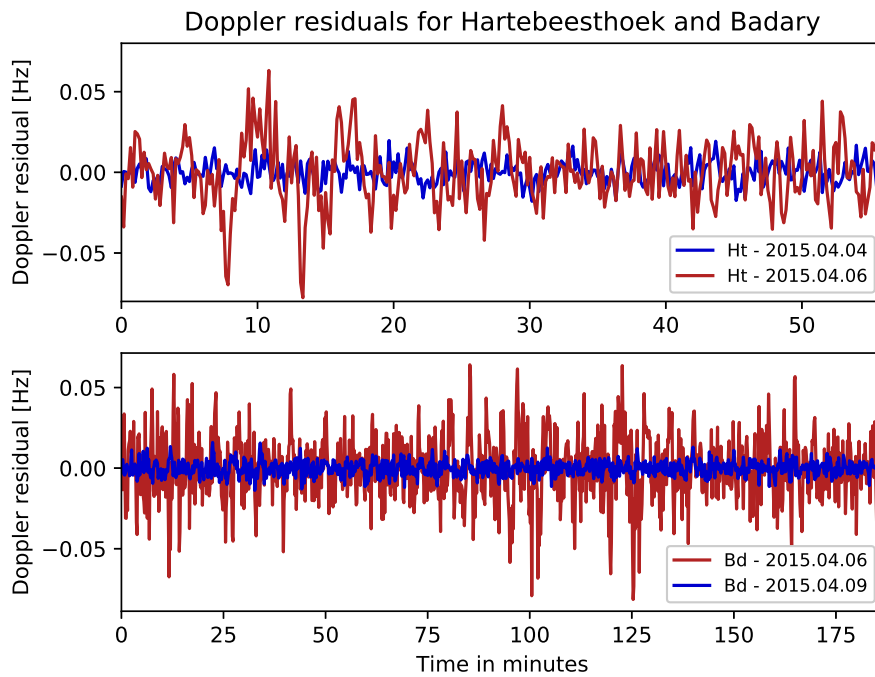


Figure 2. Doppler residuals detected at the radio telescopes of Hartebeesthoek (upper panel) and Badary (lower panel) comparing data observed during the days around the ICME. Data during the ICME on 2015.04.06 are shown in red. Data observed on 2015.04.04 and on 2015.04.09 are in blue. The initial time on the graph corresponds to the start of the observation, as specified in Table 1.

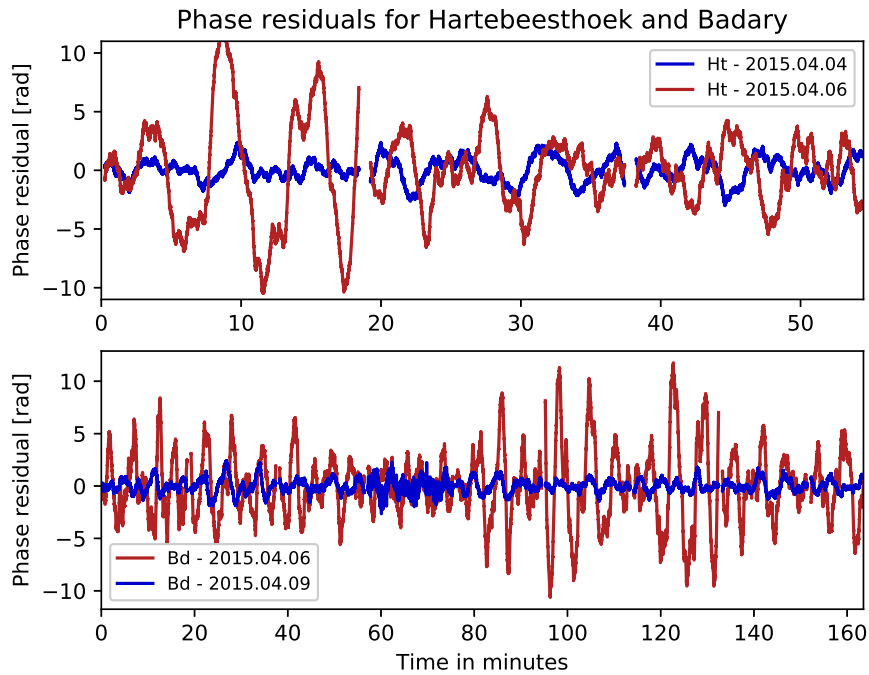


Figure 3. Phase residuals extracted from the radio telescope at Hartebeesthoek (upper panel) and Badary (lower panel) data observed during the days around the ICME. Data during the ICME on 2015.04.06 are shown in red. Data observed on 2015.04.04 and on 2015.04.09 are in blue. The initial time on the graph corresponds to the start of the observation, as specified in Table 1.

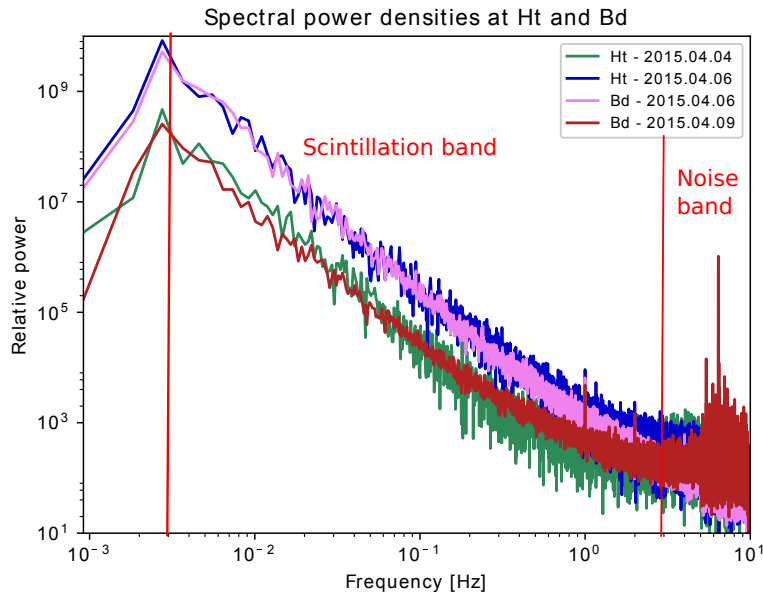


Figure 4. Comparison of the spectral power density of the phase fluctuations for sessions with the Hartebeesthoek (Ht) antenna on 2015.04.04 (green line) and 2015.04.06 (blue line), and with the Badary (Bd) antenna on 2015.04.06 (violet line) and 2015.04.09 (red line). Note that the spectral signature of the ICME has a relative power two orders of magnitude above the nominal solar wind conditions at similar solar elongations.

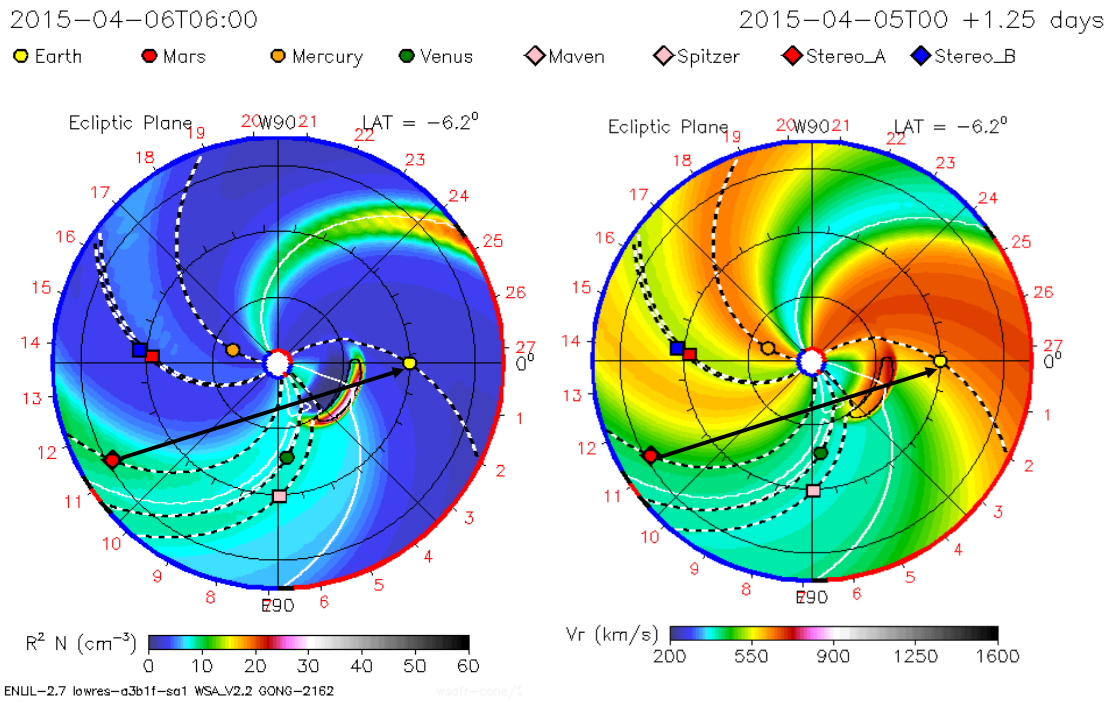


Figure 5. Geometrical configuration and plasma properties of the heliosphere when the ICME was at about 0.5 AU. (left panel) Electron density content times $R^2[N(\text{cm}^{-3})]$. (right panel) Solar wind radial speed on the elliptic plane in km/s. The simulation is for the time of our observations (2015.04.06 at 06:00 UTC). A black arrow is added to show the line-of-sight from Mars (red circle) to the Earth (yellow circle). Simulations available through the Integrated Space Weather Analysis System (iSWA, <https://ccmc.gsfc.nasa.gov/iswa/>)

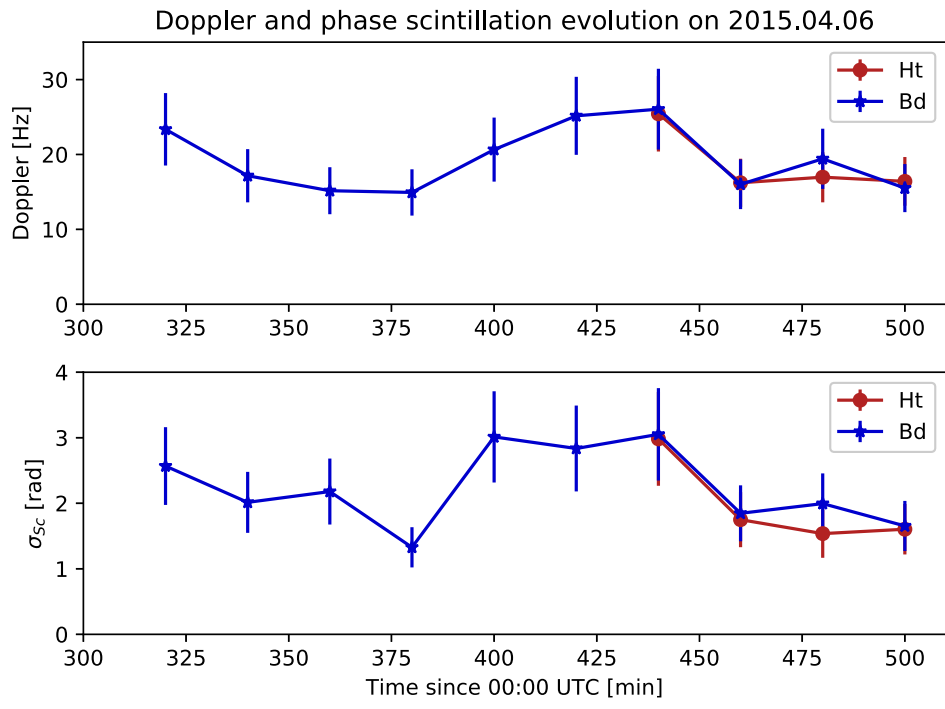


Figure 6. MEX data from 2015.04.06: (upper panel) the variability of the Doppler detection and (bottom panel) the variability of the phase scintillation for the three hours of observations. The data from the Badary (Bd) and Hartebeesthoek (Ht) stations are plotted in blue stars and red circles, respectively.

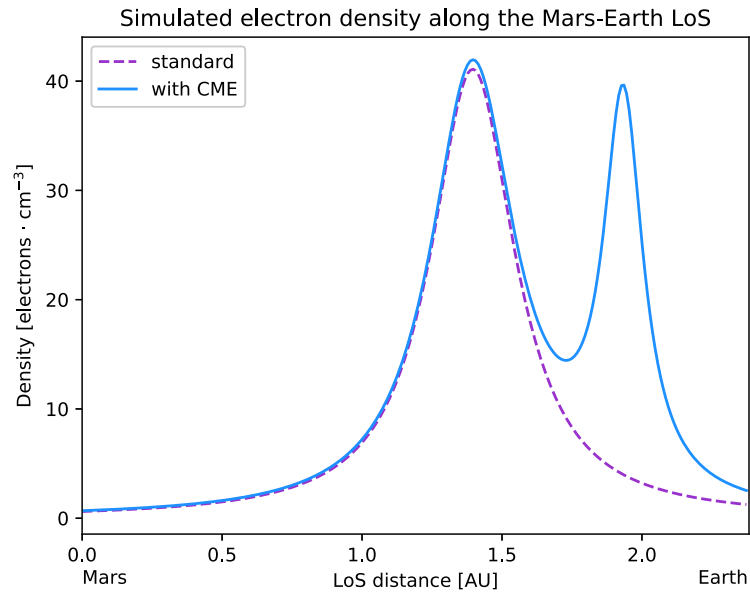


Figure 7. Electron density models of the solar wind between MEX and Earth on 2015.04.06, at 06:00 UTC. The two profiles are analytical fits of the electron density values along the line-of-sight from Mars to Earth for the TEC with and without the ICME. The dashed line shows the modelled electron density of the undisturbed solar wind ($TEC = 1350tecu$) and the solid line with the ICME ($TEC = 1950tecu$).

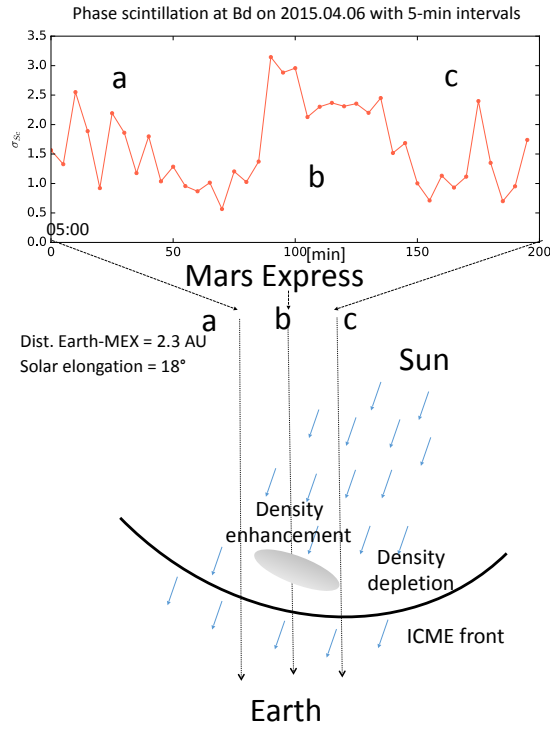


Figure 8. Sketch of the ICME based passing through the Earth-Mars line (bottom panel) and the phase variability during the full observation of MEX on 2015.04.06 at 5-min intervals, from 05:00 at the Badary station (top panel). During the entire 180 min of observation the ICME was present in the line-of-sight. A density enhancement within the ICME was encountered during the middle of the observation, shown as region (b), lasting about 60 minutes.